Article

Growth of NiAl-LDH Nanoplates on NiFe Foam and Their Enhanced Electrochemical Properties for Oxygen Evolution Reaction

Jaeyoung Lee [1,2,†], Jae Ryeol Jeong [3,†], Yoojin Lee [4,†], Jinhoon Jang [1,†], Hongdeok Park [3], Yonghwan Jo [1], Jeong Woo Han [4,*], Min Hyung Lee [3,*], and Taekyung Yu [1,*]

[1] Department of Chemical Engineering, College of Engineering, Integrated Engineering Major, Kyung Hee University, Yongin 17104, Republic of Korea
[2] School of Earth and Atmospheric Sciences, Georgia Institute of Technology, Atlanta, GA 30332, USA
[3] Department of Applied Chemistry, Kyung Hee University, Yongin 17104, Republic of Korea
[4] Department of Materials Science and Engineering, Research Institute of Advanced Materials, Seoul National University, Seoul 08826, Republic of Korea
* Correspondence: jwhan98@snu.ac.kr (J.W.H.); minhlee@khu.ac.kr (M.H.L.); tkyu@khu.ac.kr (T.Y.)
† These authors contributed equally to this work.
Received: 1 September 2025; Revised: 19 September 2025; Accepted: 29 September 2025; Published: 30 September 2025

Abstract: The development of sustainable energy that does not emit carbon pollutants is a major research topic toward minimizing waste generation and ecosystem degradation caused by the use of fossil fuels. Electrochemical water splitting is a semipermanent cycle that produces energy with zero carbon emissions. It is an innovative science and technology for a sustainable future for humanity and nature. However, its high operating potential due to the four-electron transfer process of the oxygen evolution reaction (OER) at the anode is the main factor hindering the overall reaction rate. Thus, given the importance of operating this cycle with high efficiency, studies have been extensively conducted to enhance the activity of transition-metal-based layered double hydroxide (LDH) catalysts. The use of metal foam as a substrate for LDH growth is considered the most effective method. However, most studies aimed at improving the performance of heterostructured catalysts have generally focused on controlling the active materials grown on the foam rather than the foam itself. Herein, we propose a new perspective on the role of foam, emphasizing that it is more than a mere supporting medium for growth. Density functional theory (DFT) calculations were performed to investigate the effects of NiFe foam (NFF) by modeling a heterostructure comprising NiAl-LDH and NFF. The calculation results demonstrated electron redistribution at the NiAl-LDH@NFF interface, which effectively influenced the OER performance and interfacial binding energy. Furthermore, we obtained insights into the role of foam by investigating changes in the OER overpotential caused by differences in the elements comprising the foam (Ni foam, 327 mV at 10 mA cm^{-2}; NFF, 214 mV at 10 mA cm^{-2}). This study affords flexibility in the utilization of metal foam-based heterostructured catalysts.

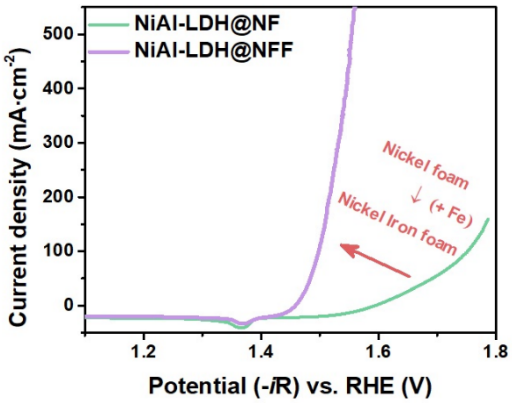

Keywords: NiFe foam; NiAl-LDH; oxygen evolution reaction; heterostructure modeling; density functional theory; substrate effect

1. Introduction

Fossil fuels have been a key resource for the advanced development of humanity worldwide. The ongoing development of highly efficient technologies for the production of shale gas has led to a continuous rise in the global production of fossil fuels [1–3]. Nevertheless, fossil fuels present a significant drawback—the substantialemission of carbon dioxide, a major contributor to global warming. Consequently, it is imperative to explore and implement clean energy alternatives for the sustainable development of humanity [4–6].

Among various eco-friendly energies, hydrogen is the most promising candidate. It is abundant on Earth, exhibits no regional scarcity, and has a higher energy density than fossil fuels. The energy density of hydrogen, petroleum, and coal is 120, 44, and 25 MJ/kg, respectively. Nevertheless, the delay in the replacement of fossil fuels by hydrogen is primarily attributed to the limited efficiency of water electrolysis, which is the predominant carbon-neutral production method for hydrogen [7]. The bottleneck is the oxygen evolution reaction (OER), a crucial half-reaction of water electrolysis characterized by inherently sluggish kinetics. Previous studies have frequently used noble-metal-based (Ru, Ir, Pt, etc.) electrocatalysts to enhance the OER efficiency [7–9]. However, these materials have failed to significantly improve the efficiency of water electrolysis, largely due to cost implications from the finite availability of noble metals. Thus, current studies have intensified their focus on materials with layered structures, particularly those comprising four-period transition metals [10–12].

Among these materials, NiAl-layered double hydroxide (NiAl-LDH) is a highly promising electrocatalyst. The incorporation of Al has been observed to be advantageous because it enhances the structural stability of Ni-based catalysts and increases the proportion of low-coordinated Ni species [13]. Furthermore, using foam as the growth environment for electrocatalysts offers significant advantages, including a high specific surface area, efficient material utilization, low mass density, versatile porous channels, and good conductivity [14–16]. The use of foam comprising well-established elements, such as Ni and Fe, which have been extensively validated, is a robust strategy for maximizing the potential of NiAl-LDH. In addition, it simultaneously addresses the limitations associated with the existing rotating disk electrode configurations.

Previous studies on electrocatalysis using density functional theory (DFT) calculations have focused on understanding the interaction between catalyst materials and their interfaces [17,18]. However, recent studies involving catalysts directly grown on substrates, such as single-atom catalysts [19,20], have revealed that changes in catalytic activity can arise from interactions between reactants and the catalyst surface, as well as from interactions between the substrate and catalyst [21–23]. Thus, this study was aimed at investigating the effect of foam on electrocatalytic reactions and examining the interface between LDH and foam. This was achieved by meticulously modeling a heterostructure comprising LDH and foam.

Herein, we present a paper detailing the direct growth of catalysts on metal foams and the resulting alterations in catalytic activity induced by the charge structure modification facilitated by the metal foam. The NiFe foam (NFF) used remarkably enhanced the catalytic activity of NiAl-LDH in the OER. The OER overpotential at 10 mA cm^{-1} using the NiAl-LDH@NFF (214 mV) as a catalyst was significantly reduced compared with that of the NiAl-LDH@Ni foam (NF) (327 mV). The activity trend was elucidated by calculating the interaction between the well-modeled NFF and NiAl-LDH. The investigation revealed that the interactions between catalysts and substrates can control the electronic structures of catalysts through charge transport from the metal substrate. This phenomenon is similar to the charge transport-induced enhancement of catalytic activity observed for single-atom catalysts. These findings provide a promising approach to the rational design of OER catalysts, wherein electronic structure control through interactions with metal substrates is leveraged at the atomic scale and at larger scales, rendering them applicable for practical implementation.

2. Experimental Section

2.1. Materials and Methods

Nickel chloride ($NiCl_2$; 98%), aluminum chloride ($AlCl_3 \cdot 6H_2O$; 99%), urea (99%), ruthenium oxide (RuO_2, 99.9%), and hydrochloric acid (HCl; 37%) were purchased from Sigma-Aldrich (St. Louis, MO, USA). NFF and NF were purchased from Medipl and 4science (Seoul, Korea), respectively. Nafion solution (D520, DuPont) was used as received. All the reagents were of analytical grade and used without further purification.

2.1.1. Synthesis of NiAl-LDH@NFF and NiAl-LDH@NF

NiAl-LDH@NFF was synthesized following a reported method that was optimized to suit the present experimental conditions [24]. The NFF (1.4 × 1.4 cm) was pretreated in HCl (3 M) for 10 min to remove the surface oxide layer. It was subsequently rinsed twice with a water and ethanol solution and dried at room temperature for 3 h. Next, $NiCl_2$ (1.6 mmol) and $AlCl_3 \cdot 6H_2O$ (0.8 mmol) were dissolved in distilled water (12 mL) with continuous magnetic stirring at 450 rpm for 10 min. Thereafter, urea (1.2 mmol) was added. The acid-treated NFF and mixed solution were transferred into a Teflon-lined stainless-steel reactor, sealed, and maintained at 120 °C for 12 h in a convection oven. Afterward, the synthesized NiAl-LDH@NFF was sonicated thrice for 2 min in a mixture of water and ethanol and dried at room temperature for future use. NiAl-LDH@NF was synthesized using the same method, except for the replacement of NFF with NF.

2.1.2. Characterization

Transmission electron microscopy (TEM) was performed using a JEM-2100F microscope (Jeol, Osaka, Japan) at 200 kV. Scanning electron microscopy (SEM) images were obtained using a LEO SUPRA 55 microscope (Zeiss, Dublin, CA, USA). Powder X-ray diffraction (XRD) patterns were recorded at room temperature using a D/MAX-2200PC X-ray diffractometer (Rigaku, Tokyo, Japan) equipped with graphite-monochromatized Cu Kα radiation (λ = 1.5418 Å). The step scan mode was employed in the 2θ range of 10–90°, with a step size of 0.02° and a counting time of 4 s per step. An inductively coupled plasma (ICP) spectrometer (Direct Reading Echelle ICP, Leeman, Hudson, NH, USA) was used to determine the Al/Ni molar ratio in the LDH. The X-ray photoelectron spectroscopy (XPS, K-Alpha, Thermo Fisher Scientific, Waltham, MA, USA) was employed to investigate the oxidation states of NiAl-LDH@NF and NiAl-LDH@NFF

2.1.3. Electrochemical Measurement

Electrochemical measurements were conducted using an SP300 electrochemical workstation (BioLogic Science Instruments, Seyssinet-Pariset, France) in a standard three-electrode configuration with a 1 M KOH electrolyte. The reference and counter electrodes were an Hg/HgO electrode and Pt mesh, respectively. To assess the electrocatalytic activity of NiAl-LDH toward OERs, linear sweep voltammetry (LSV) was performed at a sweep rate of 2 mV s^{-1}. Electrochemical impedance spectroscopy (EIS) was conducted at an amplitude of 0.01 V over a frequency range of 0.01–100,000 Hz under a bias of 0.6 V vs. Hg/HgO. The potential of the working electrode was converted into the reversible hydrogen electrode (RHE) using the following equation:

$$E_{RHE} = 0.098 + (0.0592 \cdot pH) + E_{Hg/HgO}.$$

The OER overpotential (η) was determined by subtracting 1.23 V, the theoretical potential for water oxidation, as shown in the following equation:

$$\eta = E_{RHE} - 1.23.$$

The Tafel slopes, as per the LSV curve, were fitted using the following equation:

$$\eta = a + b \log J,$$

where a represents a constant, b is the Tafel slope, and J denotes the current density. Chronopotentiometry was performed to evaluate long-term stability.

The electrochemically active surface area (ECSA) was estimated based on the electrochemical capacitance of the double layer. Cyclic voltammetry was performed to determine the capacitance of the double layer (C_{dl}) by extracting the slope of the geometric current density vs. the scan rate (5–30 mV s^{-1}). No peaks were observed in the non-Faradaic potential range of 0–0.2 vs. RHE owing to the absence of kinetic polarization. The linear slope was equivalent to twice the C_{dl}, representing the ECSA [25].

The turnover frequency (TOF) was calculated using the following equation:

$$TOF = J/(4 \times n \times F),$$

where J represents the current density at a given potential, 4 is the number of electrons transferred during the OER, n is the number of active sites of all the metal ions available for the OER (including Ni and Al), and F is Faraday's constant (96,485 C mol^{-1}) [26,27].

2.1.4. Computational Methods

Spin-polarized DFT calculations were performed using the Vienna Ab initio Simulation Package (VASP) [28,29]. The projector augmented wave (PAW) method was employed to efficiently represent the interaction between valence electrons and the ion core. The generalized gradient approximation with the Perdew, Burke, and Ernzerhof functional (GGA-PBE) was employed to describe the exchange-correlation energy [30,31]. The cutoff energy was set to 400 eV for the plane-wave expansion, and the convergence criteria were set to 0.03^{-1} and 10^{-4} eV for the residual force and energy, respectively. The Monkhorst–Pack schemes of the k-point grid for the LDH, NFF, NF slab and LDH@NFF, and LDH@NF heterostructure supercells were sampled by 2 × 2 × 1 for geometry optimization and Bader charge calculations [32].

Prior to modeling the heterostructure, NiFe(111), Ni(111) and NiAl-LDH(001) slabs were constructed. The optimized lattice parameters of the $FeNi_3$ and Ni bulks were 3.55 and 3.52 Å, respectively, similar to previous experimental and theoretical reports [33,34]. The NiFe(111) and Ni(111) surfaces were modeled with three atomic layers, where the bottom layer was fixed to describe the bulk positions. For the $Ni(OH)_2$ monoclinic bulk structure,

the optimized lattice parameters were 3.16, 3.16, and 4.64 Å for the x-, y-, and z-directions (α = β = 90°, γ = 120°), respectively. To simplify the heterostructure, the original unit cells of NiFe(111), Ni(111), and $Ni(OH)_2$ were converted into an orthorhombic unit cell. To mimic the experimental ratio of Ni and Al (Ni:Al = 3:1), NiAl-LDH was constructed by replacing one Ni atom with one Al atom in the (2 × 2) $Ni(OH)_2$ unit cell (Figure S1). For the heterostructure modeling, a (2 × 3) surface unit cell of the NiAl-LDH slab was attached to a (3 × 2) surface unit cell of NiFe(111) and Ni(111), to minimize the strain induced by the lattice mismatch. The NiFe(111) and Ni(111) slabs of the heterostructure were compressed by as much as 4.31% and 3.51% in the y-direction, respectively. The NiFe(111), Ni(111) and NiAl-LDH(001) slabs had vacuum thicknesses of 15 Å to avoid artificial interactions between its periodic images in the z-direction (Figure S2).

According to the widely accepted OER mechanism that involves the elementary steps of the four-electron mechanism, the OER occurs via three oxygen-containing intermediates as follows (Equations (1)–(4)):

$$H_2O + {}^* \rightarrow {}^*OH + H^+ + e^-, \quad (1)$$

$${}^*OH \rightarrow {}^*O + H^+ + e^-, \quad (2)$$

$$H_2O + {}^*O \rightarrow {}^*OOH + H^+ + e^-, \quad (3)$$

$${}^*OOH \rightarrow O_2(g) + {}^* + H^+ + e^-, \quad (4)$$

where the asterisk denotes an active site [35]. Under standard conditions (T = 298.15 K, p = 1 bar, pH = 0), the energy of $H^+ + e^-$ was represented by 1/2 H_2 using the standard hydrogen electrode (SHE) [36]. The Gibbs free energies of each step $\Delta G_i (i = 1, 2, 3, 4)$ were calculated by correcting the DFT energy (E) with the zero-point energy (ZPE) and entropy (S) as follows:

$$\Delta G_i = \Delta E + \Delta ZPE - T\Delta S,$$

where T = 298.15 K. The ZPE correction and S calculations used the vibrational frequencies obtained by applying the finite difference method in the DFT. The thermodynamic entropy was referenced to H_2O (g) under a pressure of 0.035 bar because it was in equilibrium with H_2O (l) at 298.15 K.

During the OER process, the step with the highest free energy change is referred to as the potential determining step (PDS). The theoretical overpotential (η) can be expressed as

$$\eta = \max(\Delta G_i)/e - 1.23\ V$$

The charge distributions of the heterostructures were evaluated using the Bader charge analysis method [37].

The interfacial binding energy between NiAl-LDH(001) and NiFe(111), Ni(111) was determined using the following equation:

$$E_b = \frac{E_{LDH@foam} - E_{LDH} - E_{foam}}{S_{interface}},$$

where $E_{LDH@foam}$, E_{LDH}, and E_{foam} denote the total energies of the LDH@foam heterostructure, LDH, and foam, respectively, and $S_{interface}$ denotes the surface area of the unit cells.

2.2. Results and Discussion

Figure 1 shows the morphology and crystal structure of NiAl-LDH@NFF prepared using an aqueous phase hydrothermal synthesis method. Figure 1a shows a low-magnification SEM image, revealing its three-dimensional macroporous structure and rough surface features. This was attributed to the formation of plate-shaped NiAl-LDH on the NFF surface. To confirm the microstructure of the NiAl-LDH@NFF, we observed the yellow dotted box in Figure 1a using field-emission (FE)SEM and measured its thickness at random points (Figure 1b). Through these measurements, we determined that NiAl-LDH nanoplates with an average thickness of 41.6 ± 7.9 nm were formed on the NFF. Figure 1c shows a TEM image of the NiAl-LDH@NFF, indicating the formation of plate morphology. This corresponds to the SEM images in Figure 1a,b. Diffraction peaks at 44.28°, 51.53°, and 75.87° from the XRD patterns of NiAl-LDH@NFF and NFF corresponded to the (111), (200), and (220) planes of $FeNi_3$ (JCPDS #38-0419), respectively (Figure 1d) [38]. Contrarily, diffraction peaks at 11.73°, 23.58°, 35.12°, and 39.71° observed for NiAl-LDH@NFF, which were not observed for NFF, could correspond to the (003), (006), (012), and (015) planes of NiAl-LDH (JCPDS #15-0087), respectively [39,40]. Based on the crystal structure analysis, it is necessary to double-check NiAl-LDH by measuring the lattice distance in the white dotted square in Figure 1c. After sufficiently increasing the magnification to investigate the lattice distance in the white dotted

square, the length of 10 spacing was measured to be 2.55 nm (Figure S3). One spacing was 2.55 Å, corresponding to the (015) plane of NiAl-LDH, evidencing the NiAl-LDH, as typically observed by high-resolution (HR) TEM [24,41]. In addition, after the hydrothermal reaction, the color of the NFF and NF changed to greenish-gray, indicating the formation of NiAl-LDH (Figure S4) [42]. The sequential comparison of low-magnification SEM images of the samples prior to (Figure S5a,b) and after the hydrothermal reaction confirmed the morphological evolution of the foam surface after the reaction (Figure S5c,d). Moreover, energy-dispersive spectroscopy (EDS) mapping images of NiAl-LDH@NFF demonstrated an even distribution of Ni, Fe, and Al on the foam surface, revealing that NiAl-LDH was well-grown on the entire NFF surface (Figure S6a).

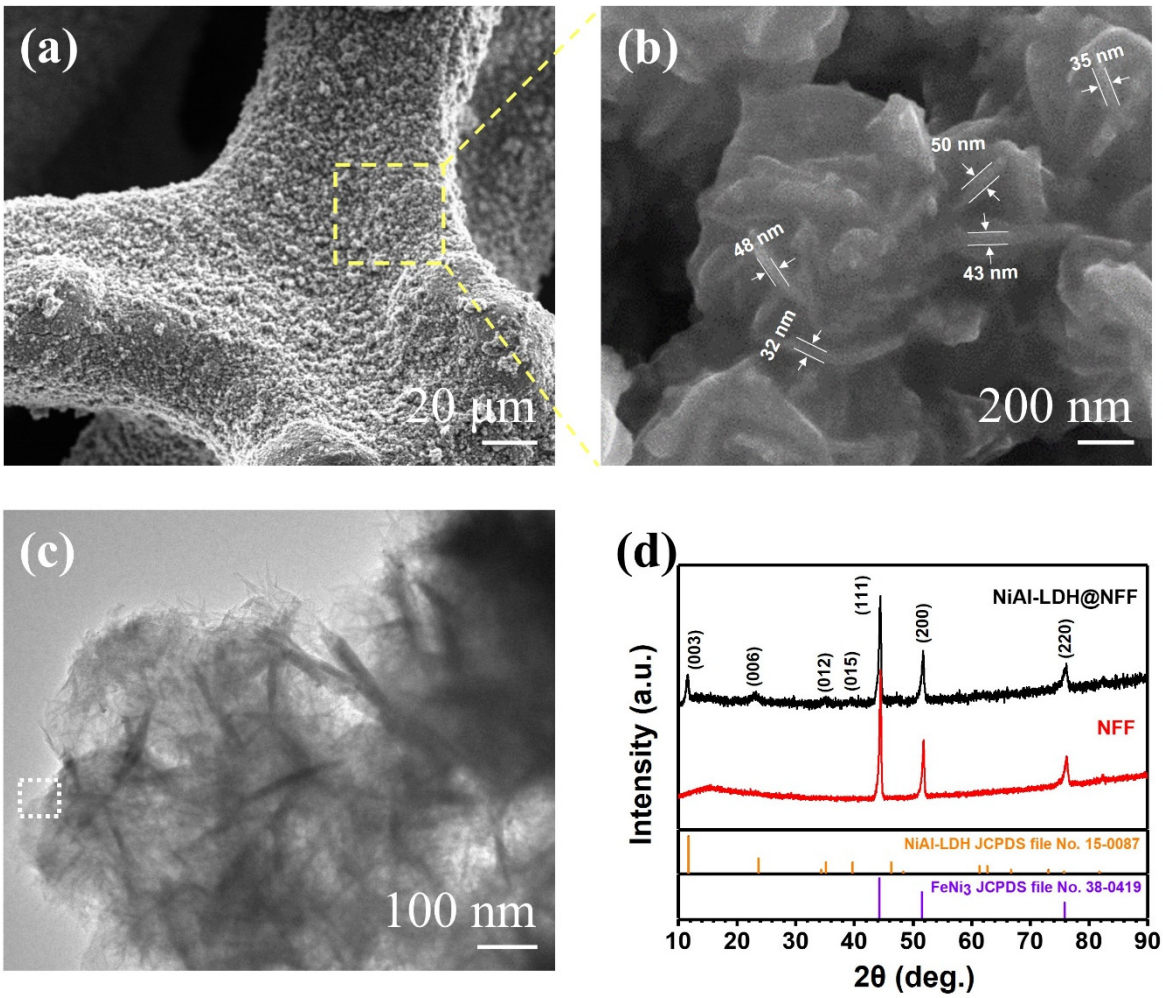

Figure 1. Characterization of NiAl-LDH@NFF. (**a**) Low (×1000) and (**b**) high (×100,000) magnification SEM images of NiAl-LDH@NFF including thickness measurements at several points. (**c**) TEM image of NiAl-LDH grown on NFF. The white dotted square corresponds to the area for measuring *d*-spacing of NiAl-LDH in Figure S3. (**d**) XRD patterns of NiAl-LDH@NFF and NFF with reference XRD patterns.

For comparison, NiAl-LDH@NF was prepared using the same synthesis method except that the procedure was conducted with NF instead of NFF. A low-magnification SEM image of NiAl-LDH@NF (Figure 2a) revealed that the foam surface was relatively smoother than that of NiAl-LDH@NFF. The average thickness of the NiAl-LDH nanoplates was 21.2 ± 2 nm, thinner than the nanoplates on NFF (Figure 2b). We believe that a relatively insufficient growth of the nanoplate could have led to the reduced thickness and blunt interface of NiAl-LDH@NF. Figure 2c shows a TEM image, indicating the formation of a small nanoplate, compared with that of NiAl-LDH@NFF, which corresponded with the SEM results (Figure 2b). The XRD patterns of NiAl-LDH@NF exhibited 44.5°, 51.85°, and 76.38° peaks corresponding to the (111), (200), and (220) planes of metallic Ni (JCPDS #87-0712), respectively (Figure 2d) [43–45]. Diffraction peaks were not observed for NiAl-LDH, potentially attributed to its low concentration on NF.

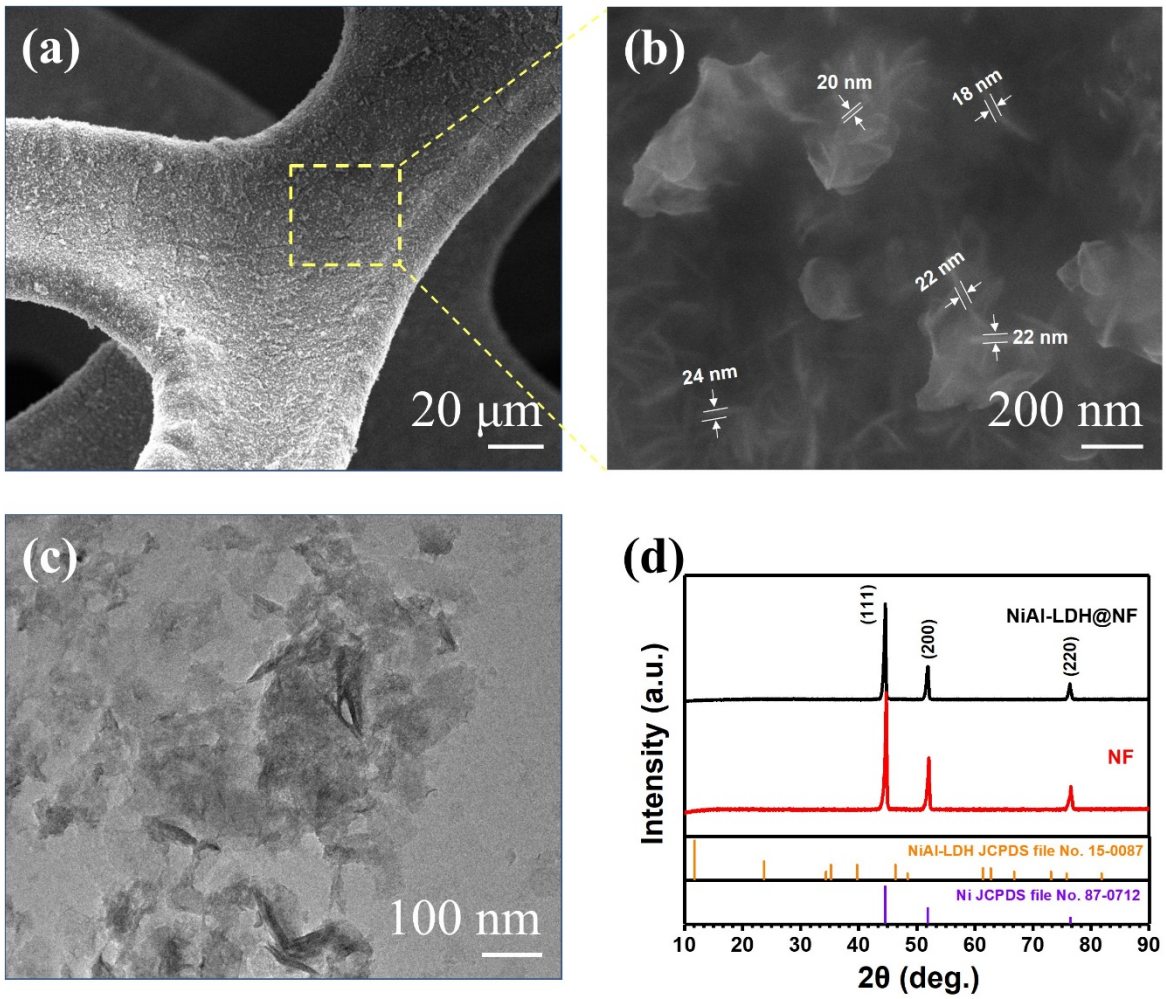

Figure 2. Characterization of NiAl-LDH@NF. (**a**) Low (×1000) and (**b**) high (×100,000) magnification SEM images of NiAl-LDH@NF including thickness measurement at several points. (**c**) TEM image of NiAl-LDH grown on NF. (**d**) XRD patterns of NiAl-LDH@NF and NF with reference XRD patterns.

However, the EDS mapping analyses confirmed that Ni and Al were evenly distributed over the entire sample area, supporting the formation of NiAl-LDH (Figure S6b). To quantitatively analyze Ni and Al in NiAl-LDH@NF, an ICP analysis was performed (Table 1). It was observed that the amount of NiAl-LDH synthesized on NF was lower than the amount of LDH on NFF. The amount of NiAl-LDH on NFF was 1.86 times that of the LDH on NF, as determined by the calculation based on Al content (0.0179 mmol for NiAl-LDH@NFF and 0.0096 mmol Al for NiAl-LDH@NF). In addition, the amount of NiAl-LDH on NF did not significantly increase when the amount of Al precursor was increased three and five times, demonstrating that the use of NFF was key in increasing the amount of NiAl-LDH on the foam (Figure S7). XPS analysis was additionally conducted to examine the oxidation states of NiAl-LDH deposited on different substrates. The Ni 2p spectra of NiAl-LDH@NF showed Ni $2p_{3/2}$ and Ni $2p_{1/2}$ peaks at 855.8 eV and 873.5 eV, respectively, while those of NiAl-LDH/NFF exhibited a slight positive shift to 856.2 eV and 874.0 eV, indicating a minor oxidation of Ni species upon changing the substrate from NF to NFF (Figure S8a). In contrast, the Al 2p binding energy decreased from 74.5 eV in NiAl-LDH@NF to 74.3 eV in NiAl-LDH@NFF, suggesting a slight reduction of Al species (Figure S8b). The Fe $2p_{3/2}$ peak at 711.3 eV confirmed the presence of oxidized Fe species (Figure S8c), while the O 1s spectra revealed contributions from M–OH groups at 531.4–531.5 eV and adsorbed H_2O near 533 eV (Figure S8d). These findings indicate that the oxidation state of NiAl-LDH is affected by the substrate, which is likely due to the NFF substrate serving as an Fe source that promotes the formation of oxidized Fe species.

To evaluate the electrocatalytic characteristics of NiAl-LDH@NF and NiAl-LDH@NFF, LSV measurements were performed. The LSV curves revealed that the overpotential of the NiAl-LDH@NFF electrode was considerably lower than that of NiAl-LDH@NF (Figure 3a). At a current density of 10 mA cm^{-2}, NiAl-LDH@NF and NiAl-LDH@NFF exhibited overpotentials of 327 and 214 mV, respectively. For comparison, the bare NF, RuO_2@NF, bare NFF, and RuO_2@NFF electrodes showed overpotentials of 400, 344, 294, and 254 mV,

respectively. Notably, NiAl-LDH demonstrated higher activity than the commercial RuO_2 catalyst, and both NiAl-LDH and RuO_2 exhibited enhanced performance when supported on NFF compared to NF. This indicated a substantial improvement in the OER activity attributable to the critical function of the NFF.

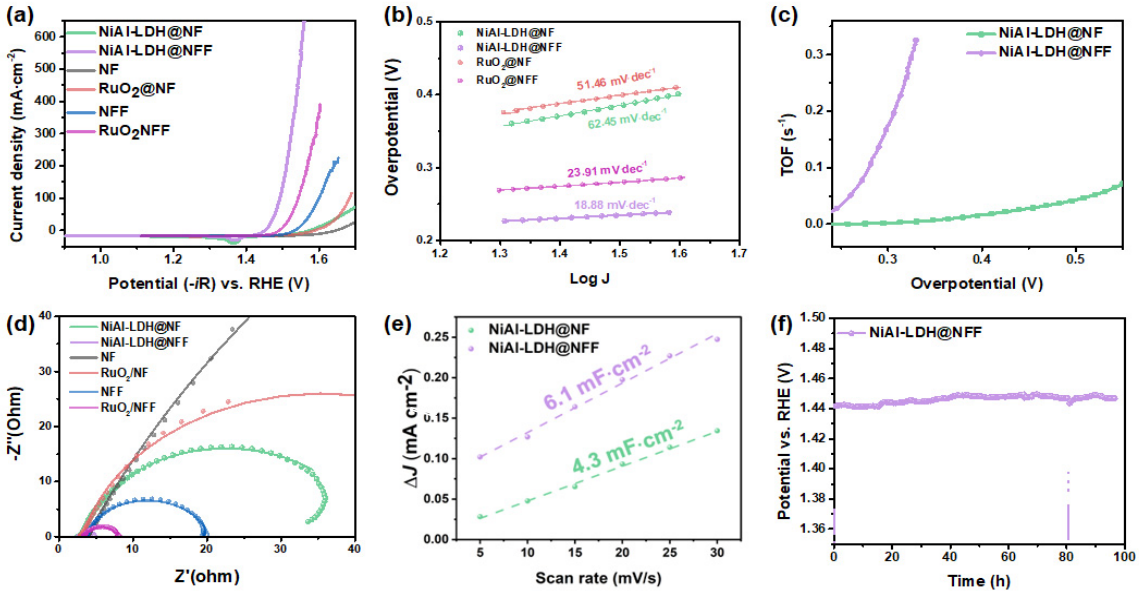

Figure 3. (**a**) LSV curves in the 1 M KOH electrolyte at a scan rate of 2 mV s^{-1}, (**b**) Tafel slopes, (**c**) TOF curves, (**d**) Nyquist plots, (**e**) linear fitting of capacitive currents of the electrocatalysts vs. scan rate, and (**f**) Chrono potentiometric stability test of NiAl-LDH@NFF recorded at a constant current density. The sharp potential drop observed around 80 h is attributed to the replenishment of electrolyte.

Furthermore, to determine the catalytic activity per amount of Ni active site, the mass activities of NiAl-LDH@NF and NiAl-LDH@NFF were investigated based on the ICP results (Table 1, Figure S9). The mass activity of NiAl-LDH@NFF exhibited an overpotential of 270 mV at 100 mA mg_{Ni}^{-1}, significantly higher than that of NiAl-LDH@NF (1.54 mA mg_{Ni}^{-1}) at the same potential.

Tafel plots derived from the LSV data were scrutinized to further assess the electrocatalytic kinetics of NiAl-LDH@NF and NiAl-LDH@NFF (Figure 3b). NiAl-LDH@NFF exhibited a significantly lower Tafel slope (18.88 mV dec^{-1}), whereas NiAl-LDH@NF exhibited 62.45 mV dec^{-1}. For comparison, RuO_2@NF and RuO_2@NFF showed Tafel slopes of 51.46 and 23.9 mV dec^{-1}, respectively. These values implied that NiAl-LDH@NFF significantly reduced the OER overpotential and augmented the reaction kinetics. The Tafel slope was substantially lower than that of other reported transition-metal-based catalysts and superior to those of noble-metal-based catalysts. This extremely low Tafel slope observed for NiAl-LDH@NFF, indicating a significantly less overpotential at a high current density, highlights its potential application as an anode for industrial-scale green hydrogen production via water electrolysis. Moreover, it can function as a counter electrode for other catalytic reactions, such as CO_2 reduction reactions.

TOF values were estimated to compare the intrinsic catalytic activities of NiAl-LDH@NF and NiAl-LDH@NFF for OERs (Figure 3c). The TOF of NiAl-LDH@NFF (0.1 s^{-1} at an overpotential of 280 mV) exceeded that of NiAl-LDH@NF (0.1 s^{-1} at an overpotential above 550 mV). This indicated an enhancement of the intrinsic catalytic properties through efficient charge transport with NFF. The EIS results corroborated the catalytic performance trend for the NiAl-LDH (Figure 3d). NiAl-LDH@NF and NiAl-LDH@NFF exhibited similar solution resistance (R_s) values of 2.5 and 2.6 W, respectively. The charge transport resistance (R_{ct}) of NiAl-LDH@NFF was significantly lower at 31.8 W, compared with that of NiAl-LDH@NF (2.3 W), corresponding with the LSV trend. In addition, the bare NF, RuO_2@NF, bare NFF, and RuO_2@NFF electrodes exhibited R_{ct} values of 340, 65, 16.7, and 4.7 Ω, respectively. These findings suggest that the NFF substrate can enhance electrical conductivity and improve charge transport, resulting in a substantially higher OER catalytic performance.

As shown in Figure 3e, the C_{dl} of the catalysts was obtained from CV curves at various scan rates within the non-Faradaic potential range (Figure S10). The C_{dl} values of NiAl-LDH@NF and NiAl-LDH@NFF were estimated at 4.3 and 6.1 mF cm^{-2}, respectively. This observation implied that the number of active sites in NiAl-LDH@NFF exceeded that in NiAl-LDH@NF.

To evaluate the durability of each catalyst, chronopotentiometry was measured at a current density of 10 mA cm^{-2} (Figure 3f). Notably, the NiAl-LDH@NFF electrode exhibited long-term stability with a slight change in potential (ΔV = 0.006 V for 97 h). The sudden potential drop observed around the 80 h mark was not indicative of catalyst degradation, but was instead a direct result of electrolyte replenishment. Furthermore, the electrochemical durability of NiAl-LDH@NFF was confirmed by TEM and XRD (Figure S11). Considering that the electrochemical reaction is fundamentally destructive, the edge of the NiAl-LDH surface became slightly blunt. However, XRD did not reveal a significant difference prior to and after the reaction, thereby demonstrating excellent stability.

Table 1. ICP analysis of NiAl-LDH@NFF and NiAl-LDH@NF.

Sample	Element	Amount (mmol)
NiAl-LDH@NFF	Ni	0.4106
	Al	0.0179
	Fe	1.3161
NiAl-LDH@NF	Ni	0.7156
	Al	0.0096

DFT calculations were performed to elucidate the origin of the improved OER activity of NiAl-LDH@NFF and to clarify the role of NFF in catalytic performance. A heterostructure model of NiAl-LDH supported on NFF was constructed and compared with that on NF, a conventional substrate for LDH synthesis (Figure 4a,b). The OER pathway was analyzed by calculating the adsorption energies of key intermediates (*OH, *O, and *OOH). The potential-determining step (PDS) was identified as the first proton-electron transfer for NiAl-LDH@NFF, in contrast to the third step for NiAl-LDH@NF (Figure 4c). The corresponding overpotentials were 0.40 eV for NiAl-LDH@NFF and 0.64 eV for NiAl-LDH@NF, demonstrating a substantial decrease of 0.24 eV in favor of the NFF-supported system. This improvement indicates enhanced OER activity, in agreement with the experimentally observed lower overpotential of NiAl-LDH@NFF.

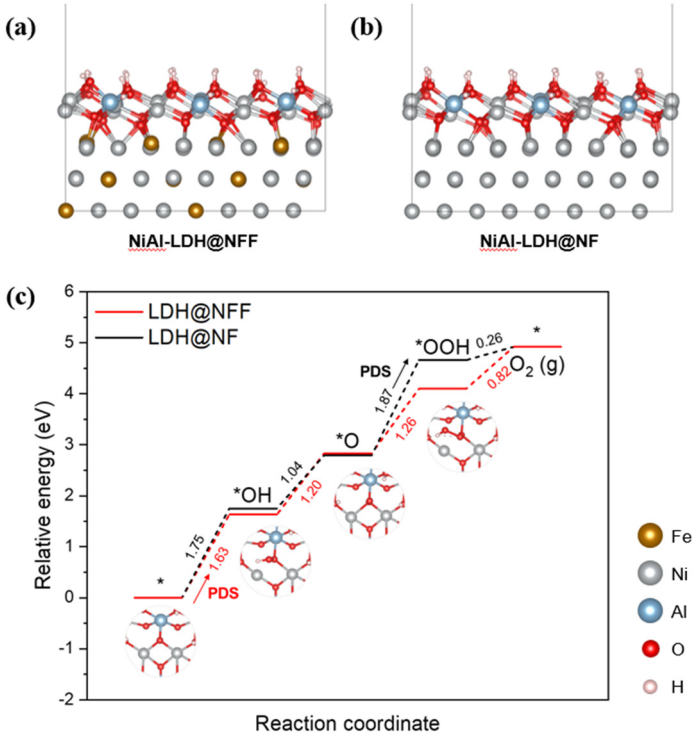

Figure 4. Model systems of (**a**) NiAl-LDH@NFF and (**b**) NiAl-LDH@NF for DFT calculations. (**c**) Gibbs energy profiles of the four-electron OER mechanism and corresponding top-view intermediate structures on the LDH@NFF surfaces. Here, PDS denotes potential-determining step.

Bader charge analysis was conducted to probe interfacial electronic interactions. In the NiAl-LDH@NFF heterostructure, Fe atoms in the foam donated electrons while Ni atoms in the NiAl-LDH layer accepted electrons. The net charge transfer to NiAl-LDH was 0.32 e^- higher in NiAl-LDH@NFF compared with NiAl-LDH@NF

(Table 2, Figure 5), indicating that Fe provides electrons to NiAl-LDH across the interface. The interfacial binding energy was further examined to assess the thermodynamic stability of the heterostructures. The calculated binding energies were −121.5 meV Å^{-2} for NiAl-LDH@NFF and −111.4 meV Å^{-2} for NiAl-LDH@NF, indicating that both foams can stabilize the NiAl-LDH layer. The more negative binding energy of NiAl-LDH@NFF suggests a stronger interfacial interaction, as reflected in the thicker growth of NiAl-LDH on NFF (Figures 1 and 2).

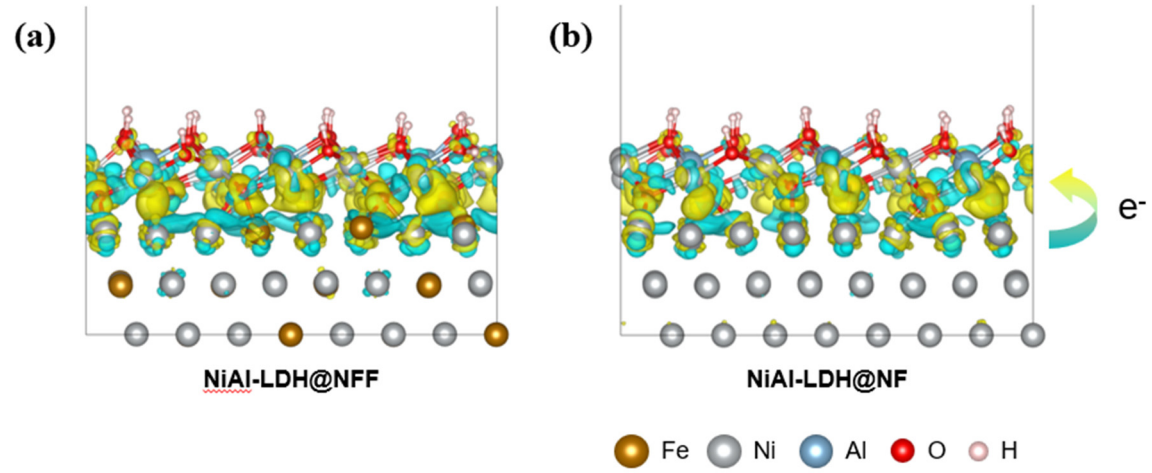

Figure 5. Charge density redistribution at the interface of NiAl-LDH and (**a**) NFF, and (**b**) NF. The yellow and cyan colors represent charge accumulation and depletion, respectively.

The number of electrons gained by LDH was 0.32 e$^-$ more in the LDH@NFF model than in the LDH@NF model, attributable to the increased supply of electrons in the foam owing to the influence of Fe. We investigated the interfacial binding energy of a heterostructure to elucidate the thermodynamic stability of the heterostructure. We calculated the interfacial binding energies of the heterostructure as −121.5 and −111.4 meV Å^{-2} for LDH@NFF and LDH@NF, respectively, indicating that NFF and NF can form stable heterostructures with NiAl-LDH. Furthermore, the stronger energy of LDH@NFF, compared with that of LDH@NF, demonstrated that a greater amount of LDH can be generated in NFF. This shows that NiAl-LDH grows thicker on NFF than on NF (Figures 1 and 2).

Table 2. Calculated Bader charge changes of Ni, Fe, and Al ions on heterostructured NiAl-LDH@NFF and NiAl-LDH@NF. The negative and positive value represents electron rich and poor, respectively.

Total Bader Charge Change			
Analyzed Component		**LDH@NFF**	**LDH@NF**
LDH	Ni	−2.37	−2.05
	Al	0.06	0.06
Foam	Ni	7.03	8.65
	Fe	2.75	-

The OER overpotential of LDH@NFF was lower than that of LDH@NF. Through the Bader charge analysis of the heterostructure on which LDH was formed on foam, it was confirmed that charge transfer occurred at the interface. More electron transfer occurred at the interface of LDH@NFF than that of LDH@NF because of the electron supply from Fe in NFF. In conclusion, it was observed that the LDH was better formed on NFF with stronger interfacial binding energy, leading to a better OER performance.

3. Conclusions

The study successfully synthesized NiAl-LDH@NFF through a hydrothermal procedure, using NFF as the growth substrate for NiAl-LDH. The heterostructured NiAl-LDH@NFF exhibited outstanding performance as an OER catalyst. Notably, NiAl-LDH@NFF exhibited a significantly denser growth (more than thrice) compared with cases where NF was employed as the growth substrate, leading to improved electrochemical performance (overpotentials of 214 and 327 mV at 10 mA cm^{-2}). DFT calculations revealed a higher electron transfer from the foam to LDH in the LDH@NFF model compared with the LDH@NF model, thereby enhancing the electrochemical performance. Moreover, the interfacial binding energy was stronger, providing evidence

supporting the enhanced LDH growth on NFF. Consequently, this study emphasized the importance of the growth substrate over the catalyst. Furthermore, this study suggests a more flexible and scalable approach in catalyst development for large-scale hydrogen generation through water electrolysis in the future, with NiAl-LDH@NFF as a promising initial step.

Supplementary Materials: The following supporting information can be downloaded at: https://media.sciltp.com/articles/others/250930153659061 9/MI-25090007-Supplementary_Materials.pdf.

Author Contributions: J.L.: Conceptualization, Data Curation, Formal Analysis, Investigation, Methodology, Writing—Original Draft Preparation; J.R.J.: Data Curation, Formal Analysis, Investigation, Methodology, Writing—Original Draft Preparation; Y.L.: Data Curation, Formal Analysis, Investigation, Methodology, Software, Writing—Original Draft Preparation; J.J.: Conceptualization, Data Curation, Formal Analysis, Investigation, Methodology, Validation; H.P.: Formal Analysis, Investigation, Methodology, Validation; Y.J.: Investigation, Validation, Writing—Review & Editing; J.W.H.: Funding Acquisition, Project Administration, Resources, Supervision, Writing—Review & Editing; M.H.L.: Funding Acquisition, Project Administration, Resources, Supervision, Writing—Review & Editing; T.Y.: Conceptualization, Funding Acquisition, Project Administration, Resources, Supervision, Writing—Review & Editing. All authors have read and agreed to the published version of the manuscript.

Funding: This work was funded by the Nano & Material Technology Development Program (RS-2024-00450102) and the Basic Research Program (RS-2021-NR059373) through the National Research Foundation of Korea (NRF) funded by the Ministry of Science and ICT. This work was (partially) funded by the BK21 FOUR program of National Research Foundation of Korea (GS-5-JO-NON-20232970). This research was (partially) funded by the BK21 FOUR program of National Research Foundation of Korea (GS-5-JO-NON).

Data Availability Statement: The authors confirm that the data supporting the findings of this study are available within the article and its supplementary materials.

Conflicts of Interest: The authors declare no conflict of interest.

References

1. Bhattacharya, M.; Paramati, S.R.; Ozturk, I.; Bhattacharya, S. The effect of renewable energy consumption on economic growth: Evidence from top 38 countries. *Appl. Energy* **2016**, *162*, 733–741.
2. Olatomiwa, L.; Mekhilef, S.; Ismail, M.S.; Moghavvemi, M. Energy management strategies in hybrid renewable energy systems: A review. *Renew. Sustain. Energy Rev.* **2016**, *62*, 821–835.
3. Chu, S., Cui, Y., & Liu, N. The path towards sustainable energy. *Nature materials*. **2017**, *16*(1), 16-22.
4. Vesborg, P.C.; Jaramillo, T.F. Addressing the terawatt challenge: Scalability in the supply of chemical elements for renewable energy. *RSC Adv.* **2012**, *2*, 7933–7947.
5. Fajrina, N.; Tahir, M. A critical review in strategies to improve photocatalytic water splitting towards hydrogen production. *Int. J. Hydrogen Energy* **2019**, *44*, 540–577.
6. Jeevanandam, J.; Barhoum, A.; Chan, Y.S.; Dufresne, A.; Danquah, M.K. Review on nanoparticles and nanostructured materials: History, sources, toxicity and regulations. *Beilstein J. Nanotechnol.* **2018**, *9*, 1050–1074.
7. Jiao, Y.; Zheng, Y.; Davey, K.; Qiao, S.Z. Activity origin and catalyst design principles for electrocatalytic hydrogen evolution on heteroatom-doped graphene. *Nat. Energy* **2016**, *1*, 16130.
8. Reier, T.; Pawolek, Z.; Cherevko, S.; Bruns, M.; Jones, T.; Teschner, D.; Selve, S.; Bergmann, A.; Nong, H.N.; Schlögl, R.; et al. Molecular insight in structure and activity of highly efficient, low-Ir Ir–Ni oxide catalysts for electrochemical water splitting (OER). *J. Am. Chem. Soc.* **2015**, *137*, 13031–13040.
9. Forgie, R.; Bugosh, G.; Neyerlin, K.C.; Liu, Z.; Strasser, P. Bimetallic Ru electrocatalysts for the OER and electrolytic water splitting in acidic media. *Electrochem. Solid-State Lett.* **2010**, *13*, B36.
10. Li, B.Q.; Xia, Z.J.; Zhang, B.; Tang, C.; Wang, H.F.; Zhang, Q. Regulating p-block metals in perovskite nanodots for efficient electrocatalytic water oxidation. *Nat. Commun.* **2017**, *8*, 934.
11. Grimaud, A.; May, K.J.; Carlton, C.E.; Lee, Y.L.; Risch, M.; Hong, W.T.; Zhou, J.; Shao-Horn, Y. Double perovskites as a family of highly active catalysts for oxygen evolution in alkaline solution. *Nat. Commun.* **2013**, *4*, 2439.
12. Karmakar, A.; Karthick, K.; Sankar, S.S.; Kumaravel, S.; Madhu, R.; Kundu, S. A vast exploration of improvising synthetic strategies for enhancing the OER kinetics of LDH structures: A review. *J. Mater. Chem. A* **2021**, *9*, 1314–1352.
13. Liu, H.; Wang, Y.; Lu, X.; Hu, Y.; Zhu, G.; Chen, R.; Ma, L.; Zhu, H.; Tie, Z.; Liu, J.; et al. The effects of Al substitution and partial dissolution on ultrathin NiFeAl trinary layered double hydroxide nanosheets for oxygen evolution reaction in alkaline solution. *Nano Energy* **2017**, *35*, 350–357.
14. Yang, G.W.; Xu, C.L.; Li, H.L. Electrodeposited nickel hydroxide on nickel foam with ultrahigh capacitance. *Chem. Commun.* **2008**, 6537–6539.
15. Li, Y.; Yang, S.; Li, H.; Li, G.; Li, M.; Shen, L.; Yang, Z.; Zhou, A. Electrodeposited ternary iron-cobalt-nickel catalyst on nickel foam for efficient water electrolysis at high current density. *Colloids Surf. A Physicochem. Eng. Asp.* **2016**, *506*, 694–702.

16. Lu, X.; Zhao, C. Electrodeposition of hierarchically structured three-dimensional nickel–iron electrodes for efficient oxygen evolution at high current densities. *Nat. Commun.* **2015**, *6*, 6616.
17. Huang, L.A.; Shin, H.; Goddard III, W.A.; Wang, J. Photochemically deposited Ir-doped NiCo oxyhydroxide nanosheets provide highly efficient and stable electrocatalysts for the oxygen evolution reaction. *Nano Energy* **2020**, *75*, 104885.
18. Huang, H.; Jung, H.; Park, C.Y.; Kim, S.; Lee, A.; Jun, H.; Choi, J.; Han, J.W.; Lee, J. Surface conversion derived core-shell nanostructures of Co particles@ RuCo alloy for superior hydrogen evolution in alkali and seawater. *Appl. Catal. B Environ.* **2022**, *315*, 121554.
19. Park, B.J.; Wang, Y.; Lee, Y.; Noh, K.J.; Cho, A.; Jang, M.G.; Huang, R.; Lee, K.S.; Han, J.W. Effective screening route for highly active and selective Metal—Nitrogen-doped carbon catalysts in CO_2 electrochemical reduction. *Small* **2021**, *17*, 2103705.
20. Liu, J.; Bak, J.; Roh, J.; Lee, K.S.; Cho, A.; Han, J.W.; Cho, E. Reconstructing the coordination environment of platinum single-atom active sites for boosting oxygen reduction reaction. *Acs Catal.* **2020**, *11*, 466–475.
21. Guo, C.; Jiao, Y.; Zheng, Y.; Luo, J.; Davey, K.; Qiao, S.Z. Intermediate modulation on noble metal hybridized to 2D metal-organic framework for accelerated water electrocatalysis. *Chem* **2019**, *5*, 2429–2441.
22. Hong, Y.R.; Dutta, S.; Jang, S.W.; Ngome Okello, O.F.; Im, H.; Choi, S.Y.; Han, J.W.; Lee, I.S. Crystal facet-manipulated 2D Pt nanodendrites to achieve an intimate heterointerface for hydrogen evolution reactions. *J. Am. Chem. Soc.* **2022**, *144*, 9033–9043.
23. Du, F.; Ling, X.; Wang, Z.; Guo, S.; Zhang, Y.; He, H.; Li, G.; Jiang, C.; Zhou, Y.; Zou, Z. Strained heterointerfaces in sandwich–like NiFe layered double hydroxides/Co1-xS for highly efficient and superior long–term durable oxygen evolution reaction. *J. Catal.* **2020**, *389*, 132–139.
24. Feng, L.; Du, Y.; Huang, J.; Cao, L.; Feng, L.; Feng, Y.; Liu, Q.; Yang, D.; Kajiyoshi, K. Nanoporous NiAl-LDH nanosheet arrays with optimized Ni active sites for efficient electrocatalytic alkaline water splitting. *Sustain. Energy Fuels* **2020**, *4*, 2850–2858.
25. McCrory, C.C.; Jung, S.; Peters, J.C.; Jaramillo, T.F. Benchmarking heterogeneous electrocatalysts for the oxygen evolution reaction. *J. Am. Chem. Soc.* **2013**, *135*, 16977–16987.
26. Anantharaj, S.; Kundu, S. Do the evaluation parameters reflect intrinsic activity of electrocatalysts in electrochemical water splitting? *ACS Energy Lett.* **2019**, *4*, 1260–1264.
27. Dang Van, C.; Kim, S.; Kim, M.; Lee, M.H. Effect of rare-earth element doping on NiFe-layered double hydroxides for water oxidation at ultrahigh current densities. *ACS Sustain. Chem. Eng.* **2023**, *11*, 1333–1343.
28. Grenier, P.; Houde, D.; Jandl, S.; Boatner, L.A. Soft-mode studies in KTa 0.93 Nb 0.07 O 3 with use of the time-resolved third-order optical susceptibility χ^3. *Phys. Rev. B* **1993**, *47*, 1.
29. Kresse, G.; Furthmüller, J. Efficient iterative schemes for ab initio total-energy calculations using a plane-wave basis set. *Phys. Rev. B* **1996**, *54*, 11169.
30. Blöchl, P.E. Projector augmented-wave method. *Phys. Rev. B* **1994**, *50*, 17953.
31. Perdew, J.P.; Burke, K.; Ernzerhof, M. Generalized gradient approximation made simple. *Phys. Rev. Lett.* **1996**, *77*, 3865.
32. Monkhorst, H.J.; Pack, J.D. Special points for Brillouin-zone integrations. *Phys. Rev. B* **1976**, *13*, 5188.
33. Pandya, N.Y.; Mevada, A.D.; Gajjar, P.N. Lattice dynamical and thermodynamic properties of $FeNi_3$, FeNi and Fe_3Ni invar materials. *Comput. Mater. Sci.* **2016**, *123*, 287–295.
34. Wang, C.; Wang, C.Y. Ni/Ni_3Al interface: A density functional theory study. *Appl. Surf. Sci.* **2009**, *255*, 3669–3675.
35. Nørskov, J.K.; Rossmeisl, J.; Logadottir, A.; Lindqvist LR, K.J.; Kitchin, J.R.; Bligaard, T.; Jonsson, H. Origin of the overpotential for oxygen reduction at a fuel-cell cathode. *J. Phys. Chem. B* **2004**, *108*, 17886–17892.
36. Valdés, Á.; Qu, Z.W.; Kroes, G.J.; Rossmeisl, J.; Nørskov, J.K. Oxidation and photo-oxidation of water on TiO_2 surface. *J. Phys. Chem. C* **2008**, *112*, 9872–9879.
37. Henkelman, G.; Arnaldsson, A.; Jónsson, H. A fast and robust algorithm for Bader decomposition of charge density. *Comput. Mater. Sci.* **2006**, *36*, 354–360.
38. Liu, G.; Wang, B.; Wang, L.; Wei, W.; Quan, Y.; Wang, C.; Zhu, W.; Li, H.; Xia, J. MOFs derived FeNi3 nanoparticles decorated hollow N-doped carbon rod for high-performance oxygen evolution reaction. *Green Energy Environ.* **2022**, *7*, 423–431.
39. Hu, X.; Li, P.; Zhang, X.; Yu, B.; Lv, C.; Zeng, N.; Luo, J.; Zhang, Z.; Song, J.; Liu, Y. Ni-based catalyst derived from NiAl layered double hydroxide for vapor phase catalytic exchange between hydrogen and water. *Nanomaterials* **2019**, *9*, 1688.
40. Zhang, X.; Chen, X.; Jin, S.; Peng, Z.; Liang, C. Ni/Al2O3 catalysts derived from layered double hydroxide and their applications in hydrodeoxygenation of anisole. *ChemistrySelect* **2016**, *1*, 577–584.
41. Jo, W.K.; Moru, S.; Tonda, S. A green approach to the fabrication of a TiO 2/NiAl-LDH core–shell hybrid photocatalyst for efficient and selective solar-powered reduction of CO_2 into value-added fuels. *J. Mater. Chem. A* **2020**, *8*, 8020–8032.
42. Koilraj, P.; Takemoto, M.; Tokudome, Y.; Bousquet, A.; Prevot, V.; Mousty, C. Electrochromic thin films based on NiAl layered double hydroxide nanoclusters for smart windows and low-power displays. *ACS Appl. Nano Mater.* **2020**, *3*,

6552–6562.

43. Yan, X.; Zhang, W.D.; Hu, Q.T.; Liu, J.; Li, T.; Liu, Y.; Gu, Z.G. Defects-rich nickel nanoparticles grown on nickel foam as integrated electrodes for electrocatalytic oxidation of urea. *Int. J. Hydrogen Energy* **2019**, *44*, 27664–27670.
44. Zhu, W.; Yue, X.; Zhang, W.; Yu, S.; Zhang, Y.; Wang, J.; Wang, J. Nickel sulfide microsphere film on Ni foam as an efficient bifunctional electrocatalyst for overall water splitting. *Chem. Commun.* **2016**, *52*, 1486–1489.
45. Wang, Z.; Wang, F.; Tu, J.; Cao, D.; An, X.; Ye, Y. Nickel foam supported hierarchical mesoporous MnO_2/$Ni(OH)_2$ nanosheet networks for high performance supercapacitor electrode. *Mater. Lett.* **2016**, *171*, 10–13.